# Crystal growth and characterization of magnetic semiconductors

Katsuaki Sato*

Department of Applied Physics, Tokyo University of Agriculture and Technology,
Koganei, Tokyo 184-8588, Japan

Magnetic semiconductors, in which spin- and charge-dependent properties of electrons coexist, has been attracting attention as the possible next-generation spin-electronics materials. This article provides a historical review of studies on crystal growth and characterization of magnetic semiconductors.

## 1. INTRODUCTION

Spintronics or electronics using spin-related phenomena has been attracting attention because of its potential applicability to new functional devices combining transport and magnetic properties. Magnetic semiconductors and ferromagnet/semiconductor hybrid structures are now the most important topics of investigation in the field of new functional semiconductor devices.

There is a long history of research on this category of materials. The first-generation materials are europium chalcogenides [1] and chalcogenides of chromium with spinel-type crystal structures [2], which were studied intensively in the late 60's and early 70's. Interesting physical properties of magnetic semiconductors, such as magnetic red shift of the absorption edge and huge negative magneto-resistance (MR) around the Curie temperature, were discovered at that time. However, researcher lost interest in these materials because their low Curie temperatures were far below the room temperature and because growth of good-quality single crystals was very difficult.

The second-generation materials are II-VI-based diluted magnetic semiconductors (DMSs), [3] among which $Cd_{1-x}Mn_xTe$ was the focus of most attention due to its capability to accommodate a high percentage of Mn atoms (as high as 77%) and its appropriate energy gap for optical application. The magnetic properties of most of these materials are either paramagnetic or spin-glass. Although the controllability of transport properties is relatively poor, the material shows a good optical property that led to its application to optical isolators.

The third-generation materials are III-V-based diluted semiconductors, in which magnetic properties have been found to be strongly dependent on the carrier concentration in the material. [4] This series of materials can only be produced by using an MBE technique with very low substrate temperatures. Since III-V compound semiconductors are widely used in electronic devices, the III-V-based DMSs are inherently capable of device-integration.

Recently, ferromagnetism in some DMS materials has been predicted by *ab-initio* calculation. A few attempts to obtain room-temperature ferromagnetism have also been reported.

Magnetic semiconductors have been discussed from the viewpoint of crystal growth in only a few reports. This paper is intended to provide a comprehensive review on crystal growth and characterization of magnetic semiconductors.

* E-mail: satokats@cc.tuat.ac.jp

## 2. FIRST-GENERATION MAGNETIC SEMICONDUCTORS

### 2.1. Chalcogenide spinels

Multinary chalcogenides with spinel structures, such as $CdCr_2Se_4$, are the most extensively studied species of magnetic semiconductor. The spinel structure belongs to the space group $Oh^7$ (Fd3m) with an fcc lattice system. The unit cell contains 8 formula units of $AB_2X_4$-type compound, where A and B are metal atoms and X is a chalcogen atom (S, Se, Te). Chemical vapor transport using halogen or halides as transporting agents was the most widely used technique for bulk crystal growth of chalcogenide spinels. The physical property of these chalcogenides and crystal growth techniques are listed in Table 1.

Exchange interaction between conduction electron spin and local magnetic moment results in various physical properties characteristic of magnetic semiconductors, such as the magnetic red shift of the band gap and the huge negative magneto-resistance in the vicinity of $T_C$ (Curie temperature). Fig. 1 shows the temperature dependence of the absorption edge in $CdCr_2Se_4$. Below the Curie temperature, the absorption edge shifts to lower energies as the temperature decreases. The temperature dependence curve of the absorption edge has been explained in terms of short-range correlation in a localized spin system.

Table 1
Physical properties of spinel chalcogenides

| Compounds | Magnetic order | Band gap (eV) | Transporting agent; Growth temperatures (°C) | Lattice parameter (nm) |
|---|---|---|---|---|
| $ZnCr_2S_4$ | AF, $T_N$=13K | | Open tube<br>Liquid transport $CrCl_3$+ZnS | 0.9974 |
| $CdCr_2S_4$ | FM, $T_C$=86K | 1.8(0K)<br>1.57(RT) | Open tube Cd+$CrCl_3$+$S_2$<br>H+Cl, 1100→1030,<br>$Cl_2$, 825→775; 825→775; 1000→750<br>$CrCl_3$, 950→900, 1000→950, 1000→750 | 1.0244 |
| $HgCr_2S_4$ | Heli, $T_N$=40K | 0.98(0K)<br>1.42(RT) | $Cl_2$,<br>900→850 | 1.0206 |
| $FeCr_2S_4$ | Ferri, $T_C$=177K | | $Cl_2$, H+Cl, 950→875<br>Open tube<br>$CrCl_3$ on FeS<br>HCl, 800→725 | 0.997 |
| $MnCr_2S_4$ | Ferri, $T_C$=71K | | $AlCl_3$, 1000→900 | 1.0045 |
| $CoCr_2S_4$ | Ferri, $T_C$=22 K | | $NH_4Cl$, 1150→1000<br>H+Cl, 1030→940<br>Liq. transport $CrCl_3$+CoS 1070→1020 | 0.990 |
| $CuCr_2S_4$ | FM, $T_C$=400K | 0 | HCl, 800→725 | 0.9629 |
| $ZnCr_2Se_4$ | Spiral AF, $T_N$=23K | 1.1(0K)<br>1.29(RT) | | 1.0443 |
| $CdCr_2Se_4$ | FM, $T_C$=130K | 1.15(0K)<br>1.32(RT) | $Cl_2$, 825→780<br>$CdCl_2$, $CdI_2$<br>$CrCl_3$, 1000→750, 800→700, 800→750 | 1.0755 |
| $HgCr_2Se_4$ | FM, $T_C$=110K | 0.32(0K)<br>0.84(RT) | $CrCl_3$, 745→670, 700→670<br>$AlCl_3$, Al+Cl, 650→625 | 1.0753 |
| $CuCr_2Se_4$ | FM, $T_C$=426K | 0 | $AlCl_3$ | 1.0357 |

Table 2

Physical properties of the divalent europium chalcogenides

| Compound | Color in reflection | Melting point (°C) | Lattice constant (Å) | Energy gap, $E_g$ (eV) | Magnetism, Transition temperature Tc(K) | Curie Weiss Temperature $\Theta_p$ (K) |
|---|---|---|---|---|---|---|
| EuO | Magenta | 2015±8 | 5.144 | 1.12 | F, 68 | 76 |
| EuS | Gold | >2320 | 5.968 | 1.65 | F,16.2 | 17 |
| EuSe | Green | >2320 | 6.195 | 1.78 | Meta | 4.6 |
| EuTe | Black | >2250 | 6.598 | 1.06 | AF | -6 |

## 2.2. Europium chalcogenides

Europium mono-chalcogenides crystallize in an NaCl-type fcc structure. They belong to the space group $Oh^5$-Fm3m. The magnetic properties of EuO and EuS are ferromagnetic with Curie temperature of 68K and 16.2K, respectively. EuSe is metamagnetic and EuTe antiferromagentic.

The physical properties of europium chalcogenides are summarized in Table 2. Since europium chalcogenides are quite refractory materials with melting points higher than 2000°C, growth from the melt is quite difficult, although not impossible. Indeed, Nakayama et al. grew EuS single crystals by a normal freezing technique using a high-pressure furnace, in which the temperature was raised above 2500 °C and vaporization of carbon heater was suppressed by Ar gas with a pressure of 300-atm.[5] Good-quality single crystals of several millimeter in size were cleaved out from the ingot. They showed a gold metallic luster suitable for optical measurements.

Growth of EuO crystals from a metal-rich solution was carried out by Schafer. [6] The reaction of sesquioxide ($Eu_2O_3$) and Eu metal proved to be the best method for producing pure EuO. However, the final product obtained by this method contains some unreacted $Eu_2O_3$. In addition, the large difference between particle sizes of the metal and the oxide often results in an inhomogeneous product in which metal particles are coated by inert $Eu_2O_3$. These difficulties can be overcome by using a quite large excess of Eu metal, i.e., of the order of 1.5 to 2 times the stoichiometric quantities.

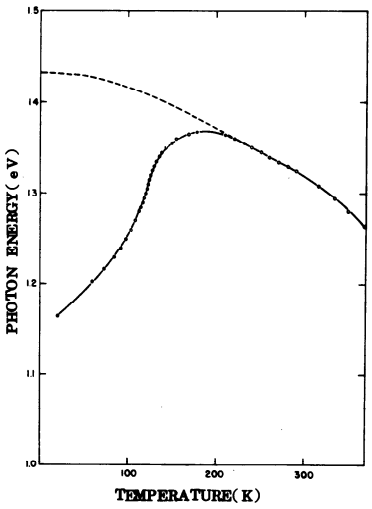


Figure 1. Temperature dependence of the energy gap (Eg) in $CdCr_2Se_4$ crystal. The dotted curve is a plot of the temperature-dependence of Eg expected for a conventional non-magnetic semiconductor extrapolated from the high-temperature part of the curve.

A mixture of Eu and $Eu_2O_3$ is pressed into slugs, which are wrapped in tantalum foil. The slugs are then slowly heated to 800°C in a closed evacuated system for 16 h. The system was evacuated down to $10^{-7}$ atm and heated to 1100°C for several hours, and all of the excess metal is distilled off due to the high vacuum.

Dimmock et al. reported the growth of single crystals by a solution method. They grew EuO in a welded tungsten crucible from a starting material consisting of Eu metal and $Eu_2O_3$ with a large metal excess. The crucible was heated to 2185°C and then cooled slowly

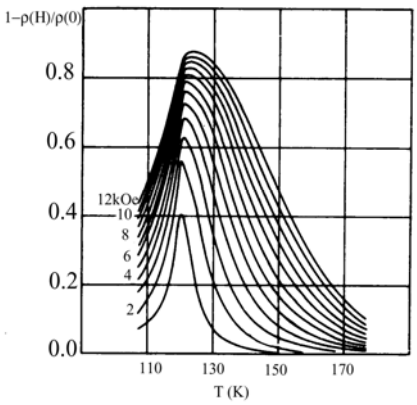


Figure 2. Negative magneto-resistance observed in $CdCr_2Se_4$ for different values of applied field.

at an initial rate of approximately 3.3°C per hour. Samples up to several millimeters in size could be cleaved from single crystalline sections. [7]

Kaldis described crystal growth of europium chalcogenides from the vapor phase. He used chemical transport for growth of EuSe and EuTe and sublimation for EuS and EuTe.[8] The vapor transport data are summarized in Table 3.

Thin films of EuS and EuO have been prepared by vacuum evaporation. Suits et al. used an EuO film as a magneto-optical recording material. [9] However, to keep the film in a ferromagnetic state, the MO-drive had to be immersed in liquid nitrogen. Efforts were therefore made to increase $T_C$. For this purpose, Fe-doped and $Eu_2O_3$-doped EuO films were examined. The films were deposited by a three-source simultaneous evaporation of $Eu_2O_3$, Eu metal and Fe metal. The substrate temperature, $T_S$, was 150°C and the vacuum during deposition was about $10^{-6}$ Torr. Film thickness was about 200 nm. The Fe content was 2 wt%. The starting ratio was 0.73 indicating that these films had been heavily doped with excess Eu, in addition to having been doped with Fe. By optimizing the temperature of annealing after deposition, a Curie temperature as high as 150 K was obtained. [10] Mitani et al. prepared thin films by vacuum evaporation on NaCl substrates. [11] Iwata et al. succeeded in epitaxial growth of an EuO film on an MgO substrate using the MBE technique. [12] The epitaxial EuO film was employed for imaging intrusion of magnetic flux into a high-temperature superconductor (HTSC).

Table 3
Crystal growth data of vapor transport for europium chalcogenides

| | $T_1$ (°C) | $T_2$ (°C) | ΔT (°C) | $I_2$ (mg/ $cm^3$) | Rate (mg/ h) | Size (mm) |
|---|---|---|---|---|---|---|
| EuTe+ $I_2$ | 1722 | 1627 | 95 | 1.35 | 18.6 | 9×8×3 |
| EuTe | 2000 | 1857 | 143 | - | 14.7 | 5×4×2 |
| EuSe +$I_2$ | 1687 | 1619 | 68 | 1.0 | 9.3 | 4×4×3 |
| EuS | 2050 | 1950 | 96 | - | 16 | 2×2×2 |

## 3. II-VI-BASED DILUTED MAGNETIC SEMICONDUCTORS

### 3.1. General description [3]

Semiconductor alloys, of which the lattice is made up in part of substitutional magnetic atoms, are called diluted magnetic semiconductors (DMS). The most extensively studied and most thoroughly understood DMS species are $A^{IIb}{}_{1-x}Mn_xB^{VI}$ alloys in which a fraction of the group IIb sublattice is replaced at random by Mn. The lattice constant and band parameters of the alloy system can be "tuned" by varying the composition of Mn. An exchange interaction between the sp-band electrons of the alloy and the localized d electrons associated with $Mn^{2+}$ results in a strongly enhanced g-value for Zeeman splitting of electronic levels, which in turn causes a strong Faraday effect near the band gap of the DMS material. The large magneto-optical effects of $Cd_{1-x}Mn_xTe$ and $Cd_{1-x-y}Hg_xMn_yTe$ are already in practical use as a Faraday rotator in optical isolators for the wavelength region in which magnetic garnet crystals are not applicable

due to presence of strong absorption. [13] The magnetic properties of most II-VI-based semiconductors are either paramagnetic or spin-glass state, properties being not very attractive for practical applications. Recently, development in novel doping technology for II-VI semiconductors has enabled to obtain p-type II-VI-based DMS materials. Theory predicts ferromagnetism in some of these DMS materials if they are heavily-doped p-type. [14]

Table 4
Crystal structure and range of composition

| Material | Crystal structure | Range of Composition |
|---|---|---|
| $Zn_{1-x}Mn_xS$ | ZB | 0<x<0.10 |
| | WZ | 0.10<x≤0.45 |
| $Zn_{1-x}Mn_xSe$ | ZB | 0<x≤0.30 |
| | WZ | 0.30<x≤0.57 |
| $Zn_{1-x}Mn_xTe$ | ZB | 0<x≤0.86 |
| $Cd_{1-x}Mn_xS$ | WZ | 0<x≤0.45 |
| $Cd_{1-x}Mn_xSe$ | WZ | 0<x≤0.50 |
| $Cd_{1-x}Mn_xTe$ | ZB | 0<x≤0.77 |
| $Hg_{1-x}Mn_xS$ | ZB | 0<x≤0.37 |
| $Hg_{1-x}Mn_xSe$ | ZB | 0<x≤0.38 |
| $Hg_{1-x}Mn_xTe$ | ZB | 0<x≤0.75 |

## 3.2. Crystal structure and composition

Crystal structures and miscibility ranges of components of ternary alloys are listed in Table 4.

Crystal structures are either of zinc-blende (ZB) or wurtzite (WZ) type. Under thermal equilibrium conditions, $Cd_{1-x}Mn_xTe$ forms an alloy of ZB structure with $x$ up to 0.77, while $Zn_{1-x}Mn_xSe$ crystallizes in ZB structure for x≤0.30 and WZ structure for 0.30<x<0.57. The ZB structure of the host II-VI compound survives for $x$ as large as 0.86 in $Zn_{1-x}Mn_xTe$.

Fig. 3 shows plots of lattice constants of telluride alloys as a function of Mn mole fraction. [15] The lattice parameter $a$ can be expressed as a function of the Mn fraction $x$ in the form

$$a = (1-x)a_{\text{II-VI}} + xa_{\text{Mn-VI}},$$

where $a_{\text{II-VI}}$ is the lattice parameter of the host II-VI compound and $a_{\text{Mn-VI}}$ is that of the "hypothetical" ZB Mn-VI compound. Note that MnS and MnSe crystallize in a cubic rock salt-type structure, while MnTe crystallizes in a hexagonal NiAs-type structure. Although the macroscopic lattice parameter determined by XRD (X-ray diffraction) follows Vegard's law, the local bond length obtained by EXAFS (extended x-ray absorption fine structure) remains practically constant throughout the entire range of compositions studied, as shown in Fig. 4 for the Mn-Se bond in $Zn_{1-x}Mn_xSe$ alloys. [16]

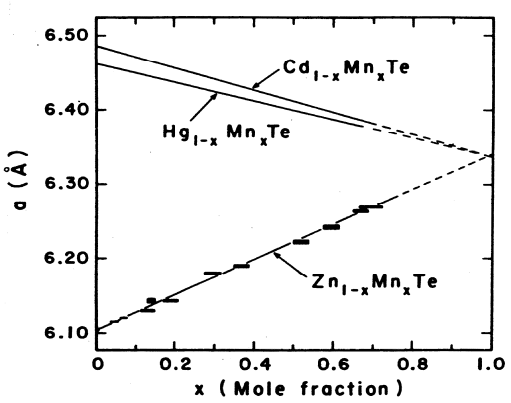


Figure 3. Lattice parameter as a function of Mn mole fraction for telluride DMS. Note that extrapolated lines converge to a single lattice constant (6.334Å), which determines the lattice parameter for the ZB phase of MnTe.

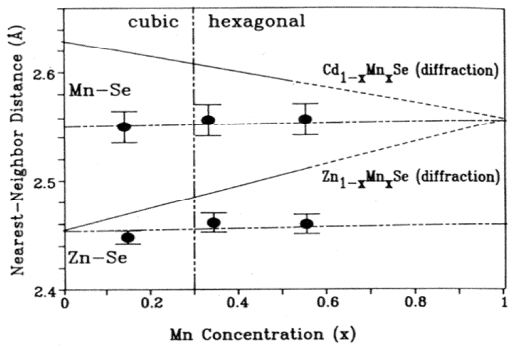


Figure 4. Actual Mn-Se and Zn-Se bond length as a function of Mn fraction determined by EXAFS. Note that either bond length has no observable change at $x$≈0.3, where $Zn_{1-x}Mn_xSe$ transforms from ZB to WZ.

### 3.3. Bulk crystal growth

Bulk single crystals of $Cd_{1-x}Mn_xTe$ for optical isolators were grown by the Bridgman technique. Elements of Cd, Mn and Te were sealed in vacuum into a quartz crucible. The crucible was lowered in a furnace to crystallize the melt through the melting point of 1100°C with a growth rate of 4 mm/h. Optical transmission of crystals often becomes poor due to twinning defects generated by the phase change from a high-temperature phase (WZ) to a low-temperature phase (ZB) during the cooling process. To obtain twin-free single crystals, Te-excess melt-composition is recommended.

The optical energy gap of a II-VI-based DMS depends linearly on the Mn concentration as shown in Fig. 5. Since a large Faraday effect of II-VI-based DMS materials is observed at photon energies close to the band gap, precise control of the composition ratio in a multinary system is required. For this purpose, recrystallization [17] and zone-melting [18] techniques of polycrystalline ingot were proposed. In order to obtain improved compositional homogeneity of a polycrystalline ingot, Onodera et al. used an quench-and-anneal technique under pressure.

### 3.4. MBE growth

Nonmagnetic II-VI thin films can be easily obtained by MBE, HWE and PLD techniques. In MBE growth, the condition for obtaining compounds stably can be adjusted, thus avoiding condensation of elements, since the vapor pressure of group II and group VI elements is relatively high compared with that of II-VI compounds. This condition is realized in CdTe for substrate temperatures between 230 and 360°C for a wide range of Cd/Te ratios. RHEED observations have revealed that the atomic arrangements of growth surfaces in Cd-excess and Te-excess conditions are different: For [001] growth, a (2×1) RHEED pattern appears under a Te-excess condition, whereas c(2×2) and (2×1) patterns appear under a Cd-excess condition, suggesting half-atomic coverage of the Cd layer on the Cd-stabilized surface. [19]

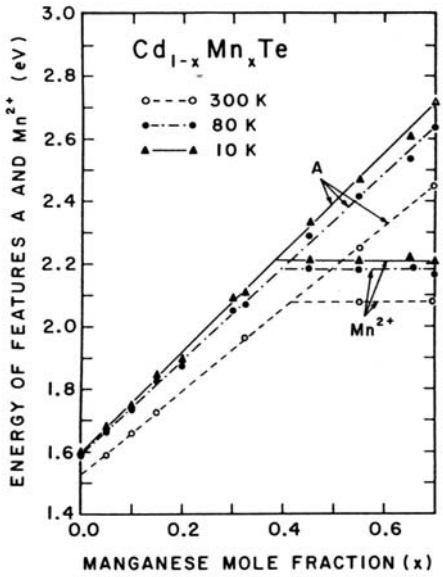


Figure 5. The optical energy gap (determined from the free exciton transition marked "A" in the figure) as a function of Mn concentration x for $Cd_{1-x}Mn_xTe$ for three temperatures.

Epitaxial growth of II-VI-based DMS using the MBE technique has been studied from mid 1980's. [20] MBE growth of $Cd_{1-x}Mn_xTe$ can easily be conducted in the same way as that of CdTe using a simultaneous supply of Mn and Cd fluxes. The addition of Mn flux does not change the growth rate under a Cd-excess condition, whereas the growth rate is increased under a Te-excess condition. The Mn composition is determined by the flux ratio of Mn/Te in the former case and by Mn/(Cd+Mn) in the latter case. [21]

Growth of high-quality $Cd_{1-x}Mn_xTe$ thin films for wave-guide-type optical isolators was achieved on a GaAs substrate by the appropriate use of ZnTe and CdTe buffer layers. [22] The transmission loss parallel to the film plane was so greatly reduced that TE-TM conversion was successfully realized using an epitaxial film.

### 3.5. Heterostructures and superlattices

Heterostructures consisting of DMS layers are expected to display many interesting and novel phenomena originating from the modulation of the exchange interaction, in addition

to the quantum confinement due to the modulation of the band gap. CdTe/$Cd_{1-x}Mn_xTe$ multiple quantum wells (MQWs) and superlattices are typical of such systems, where carriers are confined in the non-magnetic CdTe layer and their confinement potential depends strongly on the spin-states of both carriers and $Mn^{2+}$ ions in the barrier layer. This leads to magnetic field tuning of the electronic states, including the drastic phenomenon of field-induced type I→type II transition. [23]

MQW structures of DMS have been prepared on GaAs (100) substrates by MBE, HWE and ICB techniques. Kuroda et al. described MBE growth as follows: The growth was initiated by a thin buffer layer (~2000Å) followed by a $Cd_{1-x}Mn_xTe$ cladding layer (~8000Å) on the (100) surface of a GaAs substrate, and then an MQW structure consisting of 50 cycles of CdTe and $Cd_{1-x}Mn_xTe$ layers was grown and finally capped by a $Cd_{1-x}Mn_xTe$ layer of 2000 Å. [24]

### 3.6. Carrier-induced ferromagnetism in II-VI-based DMS materials

Theoreticians predict carrier-induced ferromagnetism in DMSs either by the Ruder-mann-Kittel-Kasuya-Yoshida (RKKY) mechanism or by its continuous-medium limit, the Zener model. [25]

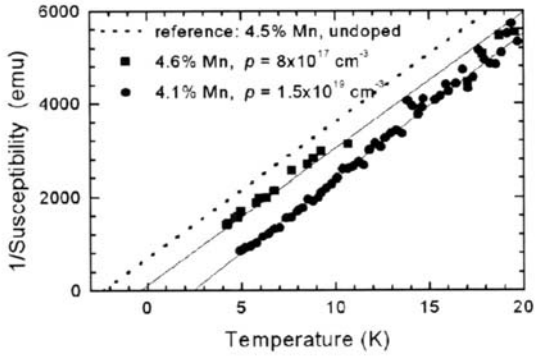


Figure 6. Inverse magnetic susceptibility (squares) for two p-$Zn_{1-x}Mn_xTe$ samples with similar Mn content $x$~0.045 but different hole concentration. Solid lines are linear fit, which serve us to determine the Curie Weiss temperature $T_{CW}$. The dotted line presents the dependence expected for an undoped sample with a similar Mn content.

Recent progress in nitrogen doping of $Zn_{1-x}Mn_xTe$ by MBE has made it possible to grow II-VI DMSs, in which the kinetic energy of holes is high enough to over-compensate electrostatic and magnetic disorder, so that the metal phase exists down to the millikelvin temperature range. In such a sample, the doping-induced ferromagnetic ordering has been realized. According to Ferrand, [26] $Zn_{1-x}Mn_xTe$:N layers were grown by MBE on an 800-μm-thick (001) Cd0.96Zn0.04Te substrate, on which a 300-nm-thick CdTe and a 200-nm-thick ZnTe buffer layer were deposited. The thickness of the ZnTe layer is larger than the critical thickness of the ZnTe/CdTe system. The $Zn_{1-x}Mn_xTe$ layer was deposited either by using stoichiometric Zn/Te flux from a ZnTe load and simply adding an Mn flux during growth or by using a Zn-rich flux, resulting in a rather rough surface or a smooth surface, respectively. An electron cyclotron resonance (ECR) plasma cell was used for the doping of atomic nitrogen. A hole concentration as high as $1.2\times10^{20}$ $cm^{-3}$ was obtained in the case of ZnTe and $Zn_{0.981}Mn_{0.019}Te$ epilayers. The magnetic properties of the $Zn_{0.981}Mn_{0.019}Te$ film were ferromagnetic with a $T_{CW}$ (magnetic transition temperature determined by the Curie-Weiss law) of 1.4 K. The value of $T_{CW}$ depends on the concentration of holes. As shown in Fig. 5, inverse magnetic susceptibility is different for two p-type $Zn_{1-x}Mn_xTe$ samples with similar Mn concentrations (x~0.045) but different hole concentrations. A doping-induced positive shift of $T_{CW}$ is clearly visible, as instead of $T_{CW}$ =-2.3K estimated for x~0.045, the observed values of TCW are 2.4 K and -0.4 K for $p=1.5\times10^{19}cm^{-3}$ and $p=7\times10^{17}$ $cm^{-3}$, respectively.

## 4. III-V-BASED DILUTED MAGNETIC SEMICONDUCTORS

### 4.1. General description [4]

Although great efforts have been made to obtain highly conductive p- and n-type materials, realization of ferromagnetism in a II-VI-based DMS with a reasonable value of $T_C$ is still difficult, and the material is therefore

not so attractive as a material for spintronic devices. III-V compounds are more suitable than II-VI compounds for electronic applications because they possess better controllability of electrical transporting properties. This fact prompted scientists to study III-V-based DMS materials. In 1989, Munekata et al. made the first attempt to fabricate a III-V-based DMS on $In_{1-x}Mn_xAs$ semiconductor alloy by means of a low-temperature MBE method. [27] Their work gained further attention when they found hole-induced ferromagnetism in p-type $In_{1-x}Mn_xAs$. [28] The Curie temperature was found to increase with hole concentration to give the highest $T_C$ of 110 K in $Ga_{1-x}Mn_xAs$ with x=0.05. [29] Owing to the advanced technology for fabrication and manipulation of good quality films and multiplayer structures, a number of interesting studies have been conducted in fundamental physics based on device-structures; for example, spin-injection LED and gate-voltage controlled ferromagnetism. [30]

## 4.2. Structure and growth technique

Generally speaking, the equilibrium solubility of transition elements in III-V compounds is as low as $10^{17}cm^{-3}$, which is far below the level (hopefully of the order of a few %) required to show (if any) a magnetic ordering effect. Vapor growth methods such as MBE seem to enable the doping of magnetic ions in excess of the thermodynamic solubility limit, since the growth method is not the equilibrium condition used for determining the solubility. Nevertheless, incorporation of a high concentration of transition atoms by MBE often leads to roughened surfaces due to surface segregation of the impurity that occurs during growth. Low-temperature MBE (LT-MBE) deposition is considered to be effective for preventing the segregation effect, because the staying time of impurity atoms on the surface is prolonged. Low temperature growth also has the merit of preventing reaction between the magnetic ions and the host elements. However, a very low growth temperature suppresses epitaxial growth, resulting in the formation of polycrystalline films. Therefore, the optimum growth temperature should be determined so as to satisfy the following two conditions: suppression of surface segregation and capability of epitaxial growth. The LT-MBE method with a substrate temperature $T_s$ of even less than 300°C ha given good results for the growth of $In_{1-x}Mn_xAs$ and $Ga_{1-x}Mn_xAs$.

### 4.3. Growth of $In_{1-x}Mn_xAs$ [31]

LT-MBE growth of $In_{1-x}Mn_xAs$ is carried out either directly on a GaAs (100) substrate that has a 7% lattice mismatch or on the buffer layer of InAs or $Al_{1-x}Ga_xSb$ that lattice-matches with the epilayer. The substrate temperature used is 200-300°C. If $In_{1-x}Mn_xAs$ layers are grown directly on a GaAs substrate with a thickness larger than 1 μm, both n-type and p-type conduction occurs in the obtained layer. The conduction type depends on $x$ and $T_s$; p-type conduction occurs at Ts>275°C for x<0.03, while n-type conduction occurs at $T$s <275. When Ts is below 200°C, polycrystalline growth occurs. On the other hand, thin layers (<30 nm) of $In_{1-x}Mn_xAs$ grown pseudomorphically on thick buffer layers are p-type at $T_s$ of less than 270°C for x>0.1. In this Mn concentration region, higher Ts results in the segregation of NiAs-type MnAs compounds.

### 4.4. Growth of $Ga_{1-x}Mn_xAs$

Ohno succeeded in LT-MBE growth of $Ga_{1-x}Mn_xAs$ using solid sources of the constituent elements. Epitaxial films of $Ga_{1-x}Mn_xAs$ were grown on semi-insulating (001) GaAs substrates at a growth rate of 0.6 μm/h. Reflection high-energy electron diffraction (RHEED) patterns were used to monitor the surface reconstruction during growth. Appropriate buffer layers such as GaAs or $Al_{1-x}Ga_xAs$ were deposited prior to growth of $Ga_{1-x}Mn_xAs$. In order to control the strain introduced by the lattice mismatch, a strain-relaxed $In_{1-x}Ga_xAs$ buffer layer with a lattice parameter value larger than the subsequent $Ga_{1-x}Mn_xAs$ layer can be employed.

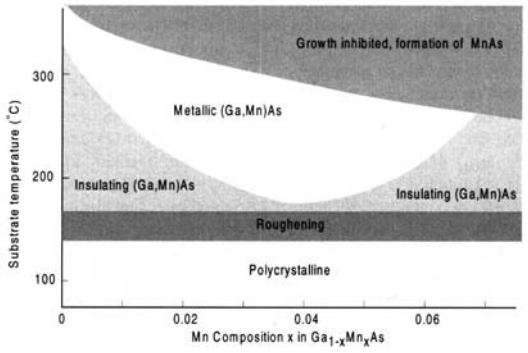


Figure 7 Phase Diagram showing the relation between growth parameters and the properties of $Ga_{1-x}Mn_xAs$ grown by MBE

Fig. 7 shows a schematic phase-diagram of MBE growth of the GaAs-MnAs system. [32] In the case of a high Mn-content $x$ exceeding a critical value or in the case of a high substrate temperature, a spotty RHEED pattern due to MnAs with a hexagonal NiAs structure appears (heavily shaded region in Fig. 7). The MnAs is a metallic ferromagnet with $T_C$=310 K. The spotty RHEED pattern suggests an island growth of MnAs. Preferable growth of a ferromagnetic $Ga_{1-x}Mn_xAs$ layer occurs in the case of a substrate temperature of ~250 and Mn content of $1\% \le x \le 7\%$. The maximum value of the Mn fraction that provides homogeneous incorporation is 7-8%, above which MnAs crystals precipitate on the surface. The electrical properties of the obtained $Ga_{1-x}Mn_xAs$ vary depending on the composition and temperature. Films are insulating when prepared under the condition shown by the lightly shaded region in Fig. 7, while they are metallic for the white region.

In the case of extremely low temperatures ($T_s$<140 °C), the RHEED pattern becomes spotty again, showing island growth, which in turn results in a ring-like RHEED pattern, suggesting the formation of a polycrystalline material.

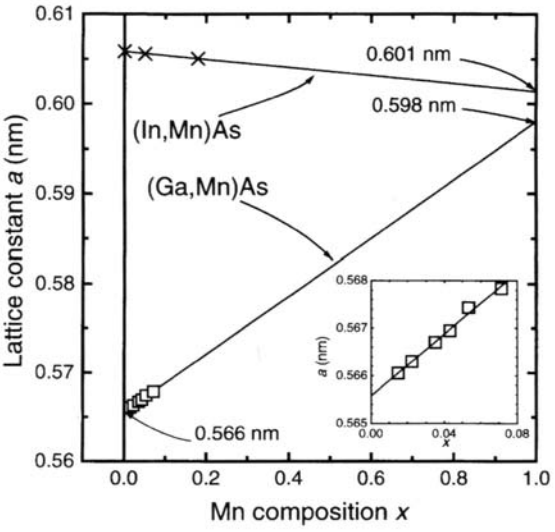


Figure 8. Relaxed lattice constant $a$ versus Mn composition $x$ in $Ga_{1-x}Mn_xAs$ films. $a$ was calculated from the X-ray diffraction peaks at room temperature, assuming that Ga1-xMnxAs layers are fully strained and that $Ga_{1-x}Mn_xAs$ has the same elastic constant as GaAs.

### 4.5. Structural and magnetic characterization

The lattice parameter $a$ of $In_{1-x}Mn_xAs$ and that of $Ga_{1-x}Mn_xAs$ are plotted as a function of Mn content $x$ in Fig. 8. [33] The lattice parameter of $Ga_{1-x}Mn_xAs$ was determined from the X-ray diffraction (XRD) assuming that $Ga_{1-x}Mn_xAs$ is fully strained and has the same elastic constant with a GaAs underlayer, while that of $In_{1-x}Mn_xAs$ was determined under the

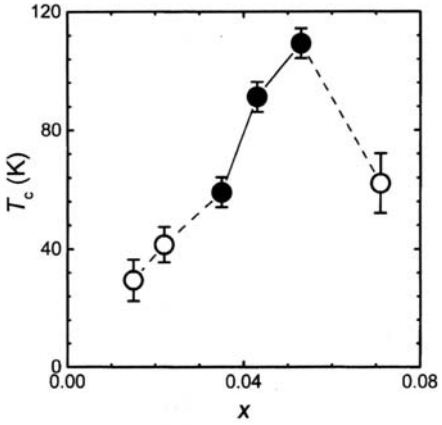


Figure 9. Ferromagnetic transition temperature TC determined from magnetotransport measurements as a function of Mn composition x. Closed circles show metalliv samples,whereas open circles show insulating samples.

assumption that the lattice is fully relaxed. As seen in the figure, the lattice parameter seems to obey Vegard's law. The extrapolated lattice parameter of hypothetical ZB-MnAs determined from the $Ga_{1-x}Mn_xAs$ system ($a$=0.598 nm) is in good agreement with that determined from $In_{1-x}Mn_xAs$ ($a$=0.601 nm). From the temperature dependence curve of the saturation magnetization determined from transport measurements in $Ga_{1-x}Mn_xAs$ with $x$=0.053, $T_C$ is determined to be 110 K. $T_C$ is plotted as a function of Mn content $x$ in Fig. 9. For x<0.07, linear relationship between $T_C$ and $x$ holds as expressed by $T_C$=2000$x$±10 K. The decrease is attributed to the beginning of partial segregation of the MnAs phase. [4]

### 4.6. Attempts to increase Mn-concentration

Recently an attempt to exceed the critical value (~7%) of Mn content in MBE growth without deterioration of crystallinity was made by Misawa et al. using an alternating supply of Mn and GaAs fluxes instead of a simultaneous supply as used in the previous studies.[34] Growth of [GaAs($x$ML)/Mn($y$ML)]$_N$ stacked layers was conducted on a GaAs (001) buffer layer of 100 nm in thickness. The substrate temperature was fixed at 230°C, which provided the best surface morphology in preliminary experiments. Control of shutters for individual K-cells supplied GaAs and Mn fluxes alternately. Surface reconstruction during growth was monitored by the RHEED pattern. The surface of the buffer GaAs showed a c(4×4) pattern, which changed to (1×1) with reduction of diffraction intensity after Mn (02 to 1.1 ML) deposition. After the second GaAs layer (9 ML in thickness) had been deposited, the intensity recovered without a drastic change in the RHEED streak pattern. With repeated deposition, the streaky RHEED pattern persisted even after 350 periods of the sequence, although the surface reconstruction pattern changed to (1×2) as in simultaneous deposition. No segregation of extraneous phases was observed. Fig. 10 shows an XRD pattern of a [GaAs (9ML)/Mn(1.02ML)]$_{100}$ layer, in which diffraction lines associated with $Ga_{1-x}Mn_xAs$ can be observed with a distinct separation from that of the GaAs (001) substrate. The Mn concentration $x$ was determined to be 14% using the relationship between $a$ and $x$ shown in Fig. 8. Surface morphology observed by SEM was quite homogeneous. Based on these results, we postulate that the monolayer or sub-monolayer of Mn acts as a surfactant for the layer-by-layer growth of GaAs, suppressing the formation of three-dimensional island growth, and is finally incorporated into the lattice to form $Ga_{1-x}Mn_xAs$ with a high concentration of Mn. Magnetic measurements in these DMS films are underway.

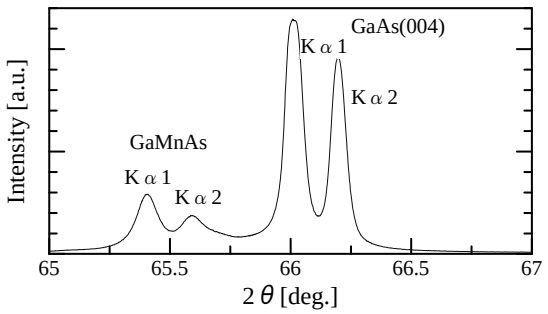


Figure 10. XRD pattern of the $Ga_{1-x}Mn_xAs$ epilayer prepared by MBE technique with alternating deposition of 100 periods of GaAs (9ML)/Mn (1.02ML) stacks

### 4.7. Heterostructure devices of III-V DMS

The use of advanced technology for hetero-epitaxy has enabled realization of spin-injection devices employing III-V DMS. Recently, Ohno et al. succeeded in fabricating an LED structure having high spin-injection efficiency. [35] Fig. 11 gives a schematic illustration of the structure. The $Ga_{1-x}Mn_xAs$ DMS is used as a spin-injector electrode. Spin-polarized electrons and unpolarized holes recombine at the $In_{1-x}Ga_xAs$ multi-quantum well (MQW) active layer, from which circularly polarized light is emitted depending on the magnetization of the DMS layer. The degree of polarization $\Delta P$ of the light emitted from the diode is plotted as a function of the applied magnetic field $B$. A considerable degree of polarization appears with a clear hysteresis loop in the magnetic-field dependence, dem-

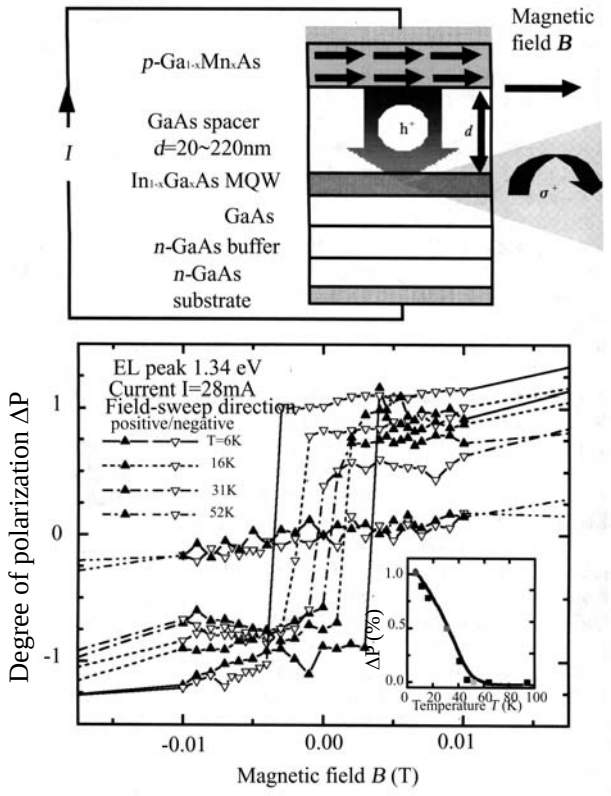


Figure 11. Electrical spin injection in pn-junction LED using ferromagnetic semiconductor $Ga_{1-x}Mn_xAs$.

onstrating the occurrence of electrical spin injection and spin transport.

A field effect transistor (FET) structure was fabricated with a thin (5 nm) $In_{0.97}Mn_{0.03}As$ layer as a channel on which a gate is formed using a polyimide as a gate insulator. By controlling the hole concentration by application of the gate voltage, carrier-induced ferromagnetism can be controlled. The change in magnetization in the channel was monitored by the Hall effect.

Fig. 12 shows Hall resistance as a function of applied field near the Curie temperature (22.5 K). The hysteresis curve dramatically changed with gate voltage. Application of negative voltage increases the magnetization as well as the in-plane anisotropy, while application of positive voltage completely reduces the coercivity.

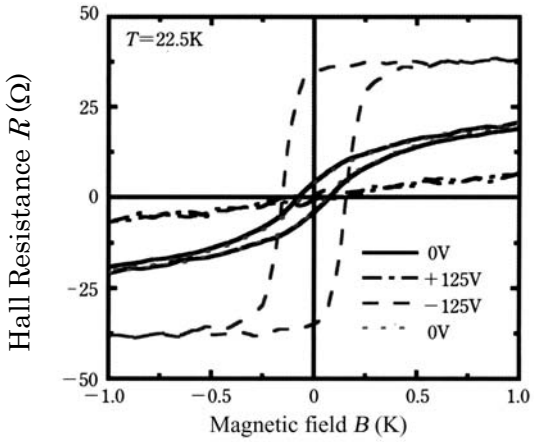


Figure 12. Gate-voltage dependence of Hall resistance in $In_{1-x}Mn_xAs$ FET.

Recently, a ferromagnetic tunnel junction device using $Ga_{1-x}Mn_xAs$/AlAs/$Ga_{1-x}Mn_xAs$ hetero-epitaxial structure was fabricated by Tanaka's group and was found to show the magneto-resistance as large as 72% as shown in Fig. 13. [36] An AlAs has thus been demonstrated to be suitable for a tunnel barrier.

## 5. FERROMAGNET/SEMICONDUCTOR HYBRIDS [37]

Ferromagnet/semiconductor hybrid structures have been attracting attention since room-temperature operation of spintronic devices is only possible at present by using such a structure. Tanaka has been investigating on epitaxial growth of various kinds of ferromagnetic films and superlattices on semiconductor substrates.

MBE growth of MnGa (tetragonal with a CuAu-type ordered structure) on GaAs was conducted using an ultrathin amorphous MnGa template (0.9 nm in thickness) deposited at a very low temperature (20-40°C). The amorphous template was heated up to 200-250°C to form a single crystalline template by solid-state epitaxy. Mn and Ga were subsequently deposited at a relatively low temperature in the range of 150-200°C and at a growth rate of 0.05 μm/h. Transmission electron microscope (TEM) observations re-

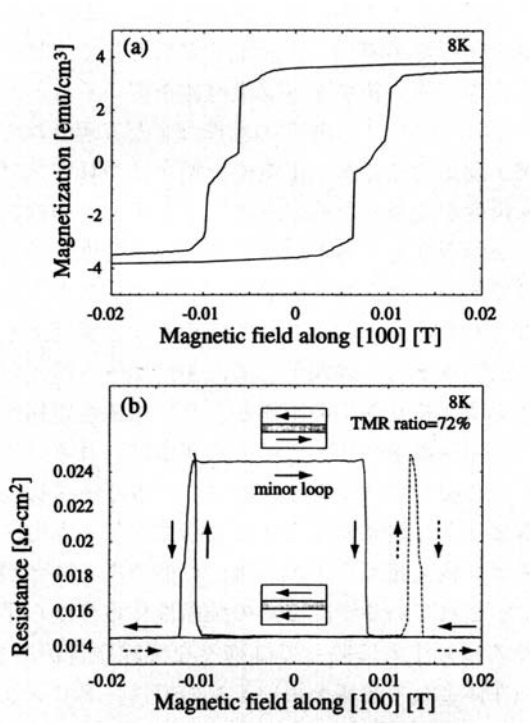


Figure 13. Tunnel magneto-resistance in $Ga_{1-x}Mn_xAs$/ AlAs/ $Ga_{1-x}Mn_xAs$ trilayer structure at 8K.

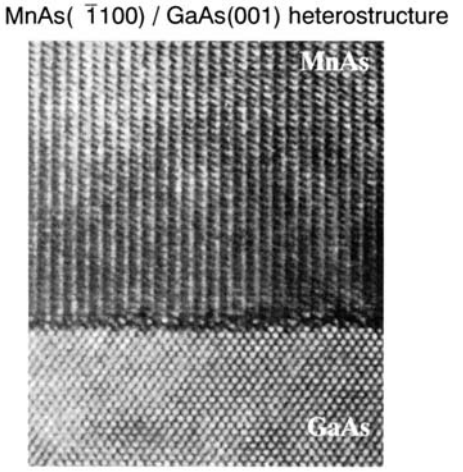


Figure 14. Cross-sectional TEM image of the MnAs/GaAs heterostructures of type-A.

vealed good epitaxial growth with a smooth and abrupt interface. The *c* parameter of the MnGa epilayer is significantly reduced from

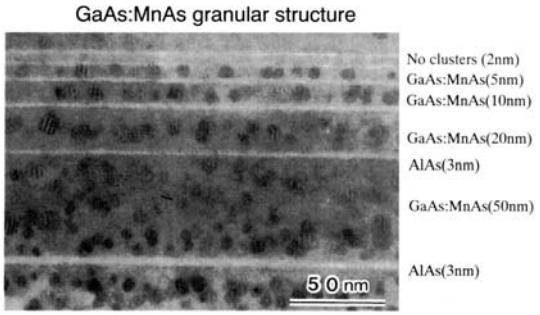


Figure 15. Cross-sectional TEM image of the GaAs:MnAs granular layers with different values of layer thickness.

that of bulk material.

Growth of NiAs-type hexagonal MnAs layers on GaAs substrates has been extensively studied by many researchers. MnAs can be deposited at 200-250°C using MBE on a GaAs (001) buffer layer of 100 nm in thickness prepared at 580°C. Tanaka showed that MBE-grown ferromagnetic MnAs thin films have two types of epitaxial orientation depending on the growth conditions. [37] In type-A, the MnAs growth plane of ($\bar{1}$100) is parallel to the GaAs (001) surface with the epitaxial relationship MnAs [11$\bar{2}$0],[0001] // GaAs [110],[$\bar{1}$10] . Fig. 14 shows a

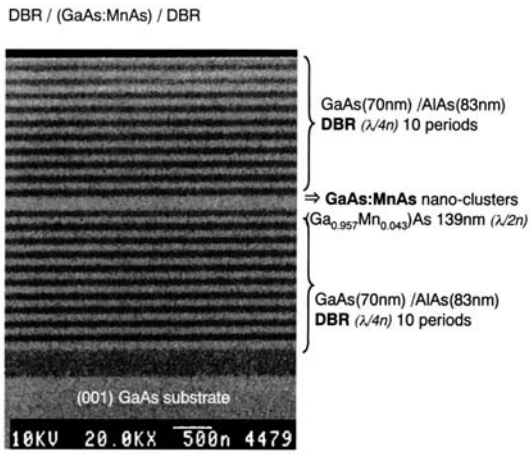


Figure 16. Photonic crystal structure consisting of GaAs:MnAs nanocluster layer sandwiched by GaAs/AlAs DBR.

cross-sectional TEM image of a type-A film. On the other hand, in type-B, $(\bar{1}101)$ is parallel to GaAs (001) with MnAs $[11\bar{2}0],[1\bar{1}02]$ //GaAs $[\bar{1}10],[110]$. A type-A film appears on the surface with disordered c(4×4), while type-B appears on a 1-ML-thick Mn layer deposited on a clean c(4×4) GaAs surface. Magnetic anisotropy differs between the two types of growth mode in relation to the substrate orientation.

Hybrid structures with granular MnAs clusters buried in GaAs have been attracting attention as possible new functional materials for spintronics and photo spinics. The granular material can be fabricated by annealing $In_{1-x}Mn_xAs$ and $Ga_{1-x}Mn_xAs$ layers at a temperature above 500°C. Segregation of nano-cluster occurs since $In_{1-x}Mn_xAs$ and $Ga_{1-x}Mn_xAs$ layers are thermodynamically in a non-equilibrium state. Fig. 15 shows cross-sectional TEM images of GaAs:MnAs granular structures for different layer thicknesses. The granular films are super-paramagnetic and have recently been found to show a large magneto-optical effect [38] and magneto- resistance. [39] Tanaka fabricated a photonic device, shown in Fig. 16, using a granular layer sandwiched by two distributed Bragg reflectors (DBRs) consisting of GaAs/AlAs multilayers. Enhancement of the Faraday effect was observed, although the Faraday rotation is still insufficient for practical use. [40]

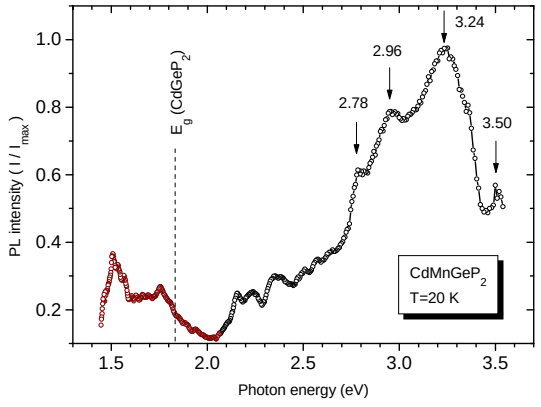


Figure 17. Photoluminescence spectrum of Mn-diffused layer on $CdGeP_2$. The excitation source is a He-Cd laser with λ=325nm. Measurement was carried out at 298K.

## 6. CHALCOPYRITE-TYPE MAGNETIC SEMICONDUCTORS

Ternary semiconductors of I-III-$VI_2$ and II-IV-$V_2$ types are ternary analogs for II-VI and III-V compounds, respectively. They crystallize in a chalcopyrite structure that belongs to the tetragonal crystal system, the unit cell of which is formed by stacking two ZB cell with an ordered arrangement of two cation atoms. The structure is the same as that of the natural mineral $CuFeS_2$, from which the name "chalcopyrite" is derived.

A number of studies have been done to substitute cations of I-III-$VI_2$ semiconductors by transition elements. The solubility of transition elements in the I-III-$VI_2$ compounds is rather poor except for $CuAl_{1-x}Fe_xS_2$ and $CuGa_{1-x}Fe_xS_2$, in which solid-solution is formed for the entire range of $x$. The magnetic properties of transition element-doped I-III-$VI_2$ semiconductors are paramagnetic or antiferromagnetic.

No systematic studies have been carried out to dope II-IV-$V_2$ compounds with transition elements. Recently, Medvedkin et al. succeeded in incorporating a high concentration of Mn atoms in a $CdGeP_2$ crystal and reported that the Mn-doped sample shows ferromagnetic behavior at room temperature. [41]

A thin Mn layer of about 30 nm in thickness was deposited at 180°C on a $CdGeP_2$ crystal in an MBE chamber using a Knudsen cell for evaporation of the Mn source, and this was followed by thermal treatment at about 500°C for 30 minutes. Prior to the deposition, the surface of the single crystal was etched with bromine-methanol solution. This treatment has been proved to be quite effective for removal of surface contamination and damage in II-VI-$V_2$ semiconductors. The RHEED pattern of the chalcopyrite structure was recovered after annealing.

Crystallographic analysis was carried out using a Rigaku RAD-IIC diffractometer, and

lattice constant change was investigated in detail using a RIGAKU RAD-B with an InP crystal monochromator.

Taking into account the ionic radii of Mn, Cd and Ge, we assume most of the Mn occupies the divalent Cd site. The Mn/Cd ratio analyzed by EDX at the surface reaches 53.4% and drops rapidly with depth, the values being 12.7% at 0.6 μm and 0.9% at 2.5 μm. The average Mn/Cd ratio was calculated to be 20% for an effective thickness of 0.5 μm.

It was found that the crystal structure of the grown layer does not strongly differ from the substrate $CdGeP_2$, except for the topmost surface, in which a texture formation was confirmed. Detailed crystallographic analysis was carried out, and it was revealed that the lattice parameter of an Mn-diffused layer is 0.8% smaller than that of the host semiconductor.

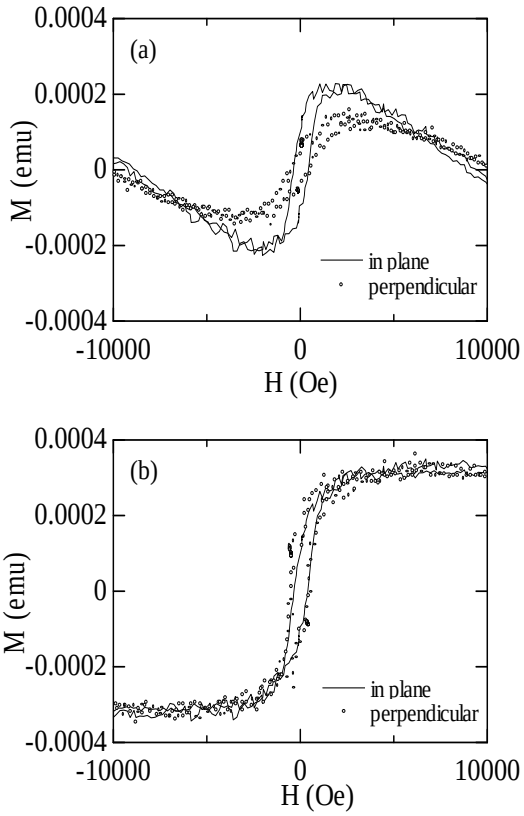


Figure 18. Magnetization curves of Mn-diffused $CdGeP_2$ layer. (a) before and (b) after correction for diamagnetic part and demagnetization field.

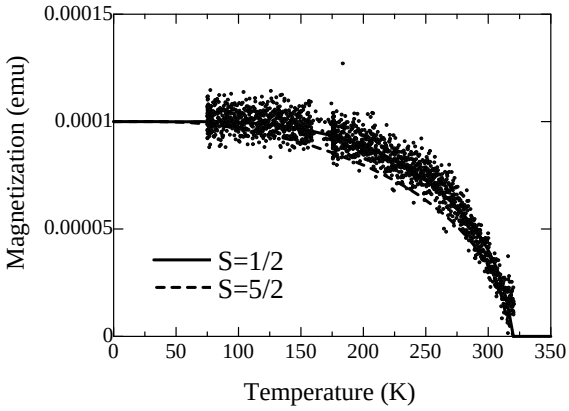


Figure 19. Temperature dependence of magnetization in the Mn-diffused $CdGeP_2$ layer.

The photoluminescence (PL) spectrum is given in Fig. 17, showing a broad emission band between 1.6 and 3.6 eV with a peak at 3.24 eV, which suggests that the new material $CdMnGeP_2$ grown on the crystal surface of a $CdGeP_2$ single crystal is also a semiconductor with an enlarged energy gap $E_g$ relative to the gap (1.83 eV) of the host semiconductor.

Magnetization was measured using a vibrating sample magnetometer (VSM) with a temperature-controlling attachment. Fig. 18(a) shows raw data of the magnetic hysteresis curves of the $CdGeP_2$:Mn system measured at room temperature (298 K). Straight lines represent in-plane magnetization, and dots represent perpendicular magnetization. The curves are clearly composed of diamagnetic and ferromagnetic components. The former may be attributed to the host substrate and the latter to the new magnetic semiconductor layer. Applying suitable corrections for diamagnetism and demagnetization fields, ferromagnetic hysteresis curves are obtained, as shown in Fig. 18(b). The ferromagnetic component shows a well-defined hysteresis loop with a saturation field $H$s of about 3 kOe and coercivity $H$c of about 0.4 kOe. The saturation magnetization at room temperature was $3.5\times10^{-4}$ emu. Assuming that deposited Mn of

30 nm in thickness on a 3×5 $mm^2$ surface area was completely incorporated into the host semiconductor, the magnetization per atomic unit was estimated to be $0.956\times10^{-20}$ emu/atom, from which the $gS$ value was determined to be 1.03 $\mu_B$. ($S$~1/2)

Fig. 19 shows a plot of remanent magnetization as a function of temperature. The curve was simulated by molecular field theory. The best fit was obtained using the Brillouin function with $S$=1/2. This fact is consistent with the spin value estimated from the saturation magnetization. The Curie temperature estimated by fitting was 320 K. [42]

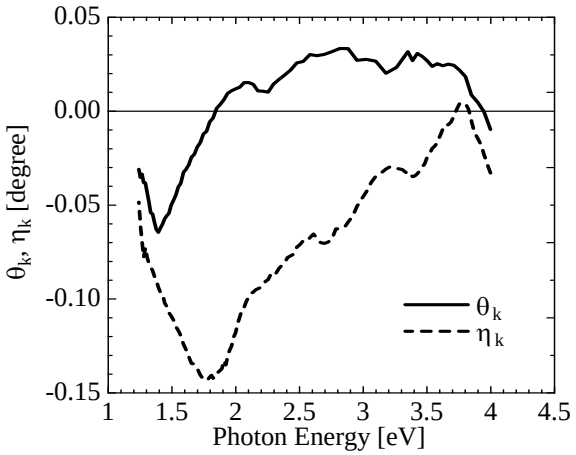


Figure 20. Spectra of magneto-optical Kerr rotation (straight line) and Kerr ellipticity (dashed line) of the Mn-diffused layer measured at room temperature.

Spectra of polar magneto-optical Kerr rotation and ellipticity measured at room temperature are shown in Fig. 20. The Kerr rotation is relatively small and is subjected to a negative peak at 1.4 eV, a zero-crossing behavior at 1.8 eV, and a few peaks between 2 and 4 eV. The peak Kerr rotation value was only 0.065 deg. On the other hand, Kerr ellipticity has a distinct negative peak at 1.75 eV and gradually approaches zero towards higher energies up to 3.8 eV, where a small positive peak appears. The energy at which the ellipticity shows a maximum coincides with the value of the energy gap of the host crystal. Specific Faraday rotation was estimated from the Kerr effect and was determined to have a value as large $5.2\times10^4$ deg/cm, which is comparable to the Faraday rotation of Bi-substituted magnetic garnet. [43]

For detailed analysis of structural characterization and explanation of electronic origin of ferromagnetism, further studies on growth of well-defined single-phase crystal and characterization of electrical transport properties are needed.

## 7. ZnO-BASED MAGNETIC SEMICONDUCTORS

Recently, the results of theoretical studies based on first-principle calculation have indicated that high $T_c$ ferromagnetism can be realized in an Mn-doped ZnO magnetic semiconductor either by RKKY [25] or double-exchange [44] mechanism. However, the Mn-doped ZnO prepared using laser-MBE by Fukumura et al. did not show ferromagnetism. [45] Since ferromagnetic interaction is mediated by a high concentration of holes, heavy p-type doping is necessary. To solve the difficulty in preparation of p-type ZnO, a co-doping process has been proposed. [46] Recently, Tabata et al. succeeded in preparation of heavily Co-doped ZnO films and found that Curie temperature is as high as 290-380 K. [47] Further studies are necessary to elucidate the mechanism of high Tc ferromagnetism in ZnO:Co.

## 8. CONCLUSIONS

Various kinds of magnetic semiconductors have been studied extensively to determine their potential as next-generation spintronics materials. Developments in epitaxial growth techniques and in doping technology have enabled us to pioneer on a new paradigm of magnetic semiconductors. Some prototype experiments show a high potential of new functional devices using spin-dependent phenomena of magnetic semiconductors.

Room-temperature ferromagnetism has been strongly required for practical applications of magnetic semiconductors. Recently,

stabilization at room temperature of carrier-induced ferromagnetism relative to antiferromagnetism has been predicted by theoretical studies. A number of experimental attempts have been made to bring the theoretical prediction into reality, and recently several groups have announced observation of room-temperature ferromagnetism in different materials, although further studies are needed to establish the electronic origin of ferromagnetism and their preparation techniques.

## ACKNOWLEDGMENTS

The author thanks Prof. Kiyotaka Sato (Hiroshima University), chairperson of the ISSCG11 committee, for his invitation to the summer school. The author also thanks Dr. Koji Ando (Electrotechnical Laboratory), Prof. S. Kuroda (University of Tsukuba) and Prof. M. Tanaka (University of Tokyo) for providing materials and manuscripts.

The studies described in this review were partially supported by grants-in-aid for scientific research from the Ministry of Education, Science, Culture and Sports of Japan, and by the Japan Society of Promotion of Science.

## REFERENCES

1. R. P. Van Stapele, *Ferromagnetic materials, vol. 3,* ed. E. P. Wohlfarth (North-Holland Publ. Co, Amsterdam, 1982) Chap.8.
2. T. Kasuya, A. Yanase, Rev. Mod. Phys. **40** (1968) 684
3. J. K. Furdyna, J. Appl. Phys. **64** (1988) R29
4. H. Ohno, J. Magn. Magn. Mater. **200** (1999) 110
5. T. Nakayama and T. Teranishi, Oyobutsuri (Bulletin of Jpn. Soc. Appl. Phys.) **39** (1970) 492
6. M.W. Schafer, J. Appl. Phys. **36** (1965) 1145
7. J.O. Dimmock, C.E. Hurwitz and T.B. Reed, Appl. Phys. Lett. **142** (1969) 49
8. E. Kaldis, J. Cryst. Growth **3-4** (1968) 146
9. J.C. Suits, IEEE Trans. Mag. **MAG-8** (1972) 421
10. J.C. Suits, K. Lee, H.F. Winters, P.B.P. Phipps and D.F. Kyser, J. Appl. Phys. **42** (1971) 1777
11. T. Mitani, M. Ishibashi and T. Koda, J. Phys. Soc. Jpn. **38** (1975) 731
12. N. Iwata, G. Pindoria, T. Morishita and K. Kohn, J. Phys. Soc. Jpn. **69** (2000) 230
13. K. Onodera, T. Matsumoto and M. Kimura, Electron. Lett. **39** (1994) 1954
14. D. Ferrand, J. Cibert, C. Bourgognon, S. Tatarenko, A. Wasiela, G. Fishman, A. Bonanni, H. Sitter, S. Kolesnik, J. Jaroszynski, A. Barcz and T. Dietl, J. Cryst. Growth **214/215** (2000) 387
15. J. K. Furdyna, W. Giriat, D. Mitchell and G. Sproule, J. Solid State Chem. **46**, (1983) 349
16. B. A. Bunker, W.-F. Pong, V. Debska, D. R. Yoder-Short and J. K. Furdyna, Diluted Magnetic (Semimagnetic) Semiconductors, ed. by R. L. Aggarwal, J. K. Furdyna, and S. von Molnár (Mater. Res. Soc., Pittsburg, PA, 1987) Vol. 89, p. 231
17. K. Onodera and H. Ohba, Cryst. Res. Technol. **31**, Suppl. (1996) 29
18. K. Onodera, *Extended Abstracts of the 55th Fall Meeting of the Japan Society of Applied Physics*, p.240 (1993)
19. S. Tatarenko, F. Bassani, J. C. Klein, K. Saminadayer, J. Cibert and V. H. Etgens, J. Vac. Sci. Technol. **A12** (1994) 140
20. S. Datta, J. K. Furdyna, and R. L. Gunshor, Superlattices and Microstructures **1** (1985) 327
21. C. Bodin, J. Cibert, W. Grieshaber, Le Si Dang, F. Marcenat, A. Wasiela, P. H. Jouneau, G. Feuiiet, D. Herve and E. Molva, J. Appl. Phys. **77** (1995) 1069
22. K. Ando, W. Zaets and K. Watanabe, Mater. Res. Soc. Symp. Proc. **517** (1999) 625
23. X. Liu, A. Petrou, J. Warnock, B. T. Jonker, G. A. Prinz and J. J. Kretz, Phys. Rev. Lett. **63** (1989) 2280
24. S. Kuroda, Y. Shirai, K. Kojima, K. Uchida, N. Miura and K. Takita, Jpn. J. Appl. Phys. **32**, Suppl. 32-3 (1993) 364.
25. T. Dietle, A. Haury and Y. Merle d'Aubigné, Phys. Rev. **B55** (1997) R3347; T. Dietle, J. Cibert, D. Ferrand and Y. Merle d'Aubigné, Mater. Sci. Eng. **B63** (1999) 103; T. Dietl, H. Ohno, F. Matsukura, J. Cibert and D. Fer-

rand, Science **287** (2000) 1019
26. D. Ferrand, J. Cibert, A. Wasiela, C. Bourgognon, S. Tatarenko and G. Fishman, Phys. Rev. **B63** (2001) 085201
27. H. Munekata, H. Ohno, S. von Molnár, A. Segmüller, L.L. Chang, L. Esaki, Phys. Rev. Lett. **63** (1989) 1849.
28. H. Ohno, H. Munekata, T. Penny, S. von Molnár, L.L. Chang, Phys. Rev. Lett. **68** (1992) 2664.
29. A. Shen, H. Ohno, F. Matsukawa, Y. Sugawara, Y. Ohno, N. Akiba, T. Kuroiwa, Jpn. J. Appl. Phys. **36**, Part 2 (1997) L73.
30. Y. Ohno, D. K. Young, B. Beschoten, F. Matsukura, H. Ohno and D. D. Awschalom, Nature **402** (1999) 790
31. H. Ohno, H.Munekata, S. von Molnár, A. Harwit, A. Segmüller, L.L. Chang, J. Vac. Sci. Technol. **B8** (1990) 176
32. A. Shen, H. Ohno, F. Matsukura, Y. Sugawara, N. Akiba, T. Kuroiwa, A. Oiwa, A. Endo, S. Katsumoto and Y. Iye, J. Cryst. Growth **175/176** (1997) 1069
33. H. Ohno, A. Shen, F. Matsukura, A. Oiwa, A. Endo, S. Katsumoto and Y. Iye, Appl. Phys. Lett. 69 (1996) 363
34. R. Misawa, T. Morishita and K. Sato, J. Jpn. Assoc. Cryst. Growth **27** (2000) 34 (In Japanese)
35. Y. Ohno, D.K. Young, B. Beschoten, F. Matsukura, H. Ohno and D.D. Awschalom, Nature **402** (1999) 790
36. Y. Higo, H. Shimizu and M. Tanaka, *Digest Int. Conf. Phys. & Appl. Spin-Related Phenomena in Semiconductors, NL-2*, Sendai, Sept. 2000.
37. M. Tanaka, Mater. Sci. & Eng. **B31**(1995) 117
38. H. Akinaga, S. Miyanishi, K. Tanaka, W. van Roy and K. Onodera, Appl. Phys. Lett. **76** (2000) 97
39. H. Akinaga, M. Mizuguchi, K. Ono and M. Oshima: Appl. Phys. Lett. **76** (2000) 357
40. H. Shimizu and M. Tanaka: *Extended Abstracts, 8th MMM-Intermag Conference, FE04*, San Antonio, Jan. 2000 p.358
41. G.A. Medvedkin, T. Ishibashi, T. Nishi, K. Hayata, Y. Hasegawa and K. Sato: Jpn. J. Appl. Phys. **39**, Part 2 (2000) L949
42. K. Sato, G. A. Medvedkin, T. Ishibashi, T. Nishi, R. Misawa, K. Yonemitsu, and K. Hirose: J. Magn. Soc. Jpn. **25** (2001) No. 4-2 (in press). (In Japanese)
43. K. Sato, G.A. Medvedkin, K. Hayata, Y. Hasegawa, T. Nishi, R. Misawa and T. Ishibashi, J. Magn. Soc. Jpn. **25** (2001) 283
44. K. Sato and H. Katayama-Yoshida, Jpn. J. Appl. Phys. **39** Part 2 (2000) L555.
45. T. Fukumura, Zhengwu Jin, A. Ohtomo, H. Koinuma and M. Kawasaki, Appl. Phys. Lett. **75**, 3366 (1999)
46. T. Yamamoto and H. Katayama-Yoshida, Jpn. J. Appl. Phys.**38**, Part 2 (1999) L166
47. H.Tabata, K. Ueda and T. Kawai, *Proc. Int. Conf. Physics and Application of Spin-Related Phenomena in Semiconductors, Sendai, September 2000*. (to be published)